Title	Electronic structure and defect physics of tin sulfides: SnS, Sn2S3, and SnS2
Authors	Yu Kumagai, Lee A. Burton, Aron Walsh, Fumiyasu Oba
Citation	Physical Review Applied, vol. 6, pp. 014009-1-14
Pub. date	2016, 7
Copyright	(c) 2016 American Physical Society
DOI	http://dx.doi.org/10.1103/PhysRevApplied.6.014009

PHYSICAL REVIEW APPLIED **6,** 014009 (2016)

Electronic Structure and Defect Physics of Tin Sulfides: SnS, Sn_2S_3, and SnS_2

Yu Kumagai,[1,*] Lee A. Burton,[2] Aron Walsh,[3] and Fumiyasu Oba[2,1]
[1]*Materials Research Center for Element Strategy, Tokyo Institute of Technology,
Yokohama 226-8503, Japan*
[2]*Laboratory for Materials and Structures, Institute of Innovative Research, Tokyo Institute of Technology,
Yokohama 226-8503, Japan*
[3]*Centre for Sustainable Chemical Technologies and Department of Chemistry, University of Bath,
Claverton Down, Bath BA2 7AY, United Kingdom*
(Received 6 May 2016; published 18 July 2016)

The tin sulfides SnS, Sn_2S_3, and SnS_2 are investigated for a wide variety of applications such as photovoltaics, thermoelectrics, two-dimensional electronic devices, Li ion battery electrodes, and photocatalysts. For these applications, native point defects play important roles, but only those of SnS have been investigated theoretically in the literature. In this study, we consider the band structures, band-edge positions, and thermodynamical stability of the tin sulfides using a density functional that accounts for van der Waals corrections and the GW_0 approximation. We revisit the point-defect properties, namely, electronic and atomic structures and energetics of defects, in SnS and newly examine those in SnS_2 and Sn_2S_3 with a comparison to those in SnS. We find that SnS_2 shows contrasting defect properties to SnS: Undoped SnS shows p-type behavior, whereas SnS_2 shows n type, which are mainly attributed to the tin vacancies and tin interstitials, respectively. We also find that the defect features in Sn_2S_3 can be described as a combination of those in SnS and SnS_2, intrinsically Sn_2S_3 showing n-type behavior. However, the conversion to p type can be attained by doping with a large monovalent cation, namely, potassium. The ambipolar dopability, coupled with the earth abundance of its constituents, indicates great potential for electronic applications, including photovoltaics.

DOI: 10.1103/PhysRevApplied.6.014009

I. INTRODUCTION

The tin-sulfide series comprises three stable compositions, namely, SnS, Sn_2S_3, and SnS_2. Because of their simple composition and earth-abundant and cost-effective constituent elements, a number of researchers are seeking suitable technological applications from physics, chemistry, and materials science viewpoints.

SnS has a layered structure (the distorted GeS structure) found as a mineral called herzenbergite and is stable in the presence of water and oxygen in the atmosphere. Of the tin sulfides, SnS is the most well studied and has been considered as a potential thin-film photovoltaic absorber because of its appropriate band gap of 1.1 eV and high optical-absorption coefficients (2×10^4 cm^{-1} above 1.3 eV) for past two decades [1,2]. Recently, Sinsermsuksakul *et al.* attained a photovoltaic efficiency over 4.4% [3]. However, this highest efficiency is far below the theoretical maximum efficiency of 24% [4,5]. SnS is known to represent an intrinsic p-type conductivity due to tin vacancies (V_{Sn}) with carrier concentrations between 10^{15} and 10^{18} cm^{-3} [1,3]. The band alignment at the heterojunctions between SnS and an n-type buffer layer [e.g., Zn(O,S) or CdS] and between SnS and a back-contact metal (e.g., Mo) is considered an issue of the low photovoltaic efficiency [3,6]. Therefore, the fabrication of SnS p-n homojunctions might overcome the limitation of photovoltaic efficiency, but the reports on n-type conductivity are still limited and controversial [2,7,8]. SnS is also studied for thermoelectric applications thanks to its low thermal conductivity and controllable carrier density by doping [9,10]. In addition, the cleaved monolayer SnS shows potential in terms of valleytronic physics [11].

SnS_2 also has a layered structure, in which S ions sandwich Sn layers hexagonally, and the layers are weakly bounded by van der Waals (vdW) interactions. At a low temperature, SnS_2 has the simplest interlayer stacking called 2H-SnS_2 (the PbI_2 structure). SnS_2 is recently well studied for the Li ion battery electrode [12,13], visible-light photocatalyst for water splitting [14], gas sensor [15], and field emitter [16]. The single SnS_2 nanosheet is also studied as a two-dimensional semiconductor material, and recently Song *et al.* fabricated field-effect transistors and related logical gates from monolayer SnS_2 [17]. SnS_2 has a larger gap of 2.3 eV, which is suited for window layer materials in thin-film photovoltaics [18]. The carrier type of undoped SnS_2 is known to be n type [18–20] and, therefore, is also a potential n-type counterpart of SnS-based solar cells. The origin of the n-type behavior, however, is not yet well described.

Sn_2S_3 has received relatively little attention in the literature so far, but herein we reveal its potential as a

---

[*] yuukuma@gmail.com

semiconductor. Specifically, Sn_2S_3 is the only well-established mixed-valence tin binary compound known. For instance, the fabrication of Sn_3O_4 and SnN is still challenging experimentally [21,22], whereas Steinmann *et al.* report that purchased SnS contains as much as 55% of Sn_2S_3 by weight [23], indicating that Sn_2S_3 is easy to make. Since the atomic framework is composed of a combination of SnS and SnS_2 structures, the electronic structure is expected to be their superposition. The band gap is around 1.1 eV [18], which is close to that of SnS, but the carrier is considered *n* type [18], in contrast to SnS. Since lone-pair electrons commonly exist in both SnS and Sn_2S_3, the valence-band position of Sn_2S_3 is expected to be close to that of SnS. Thus, the carrier type may be inverted to *p* type, allowing the fabrication of *p*-*n* homojunctions. Given the appropriate band gap, Sn_2S_3 has great potential as a solar-cell material. Indeed, the reported absorption coefficient immediately above the band gap is $7 \times 10^3\ \mathrm{cm}^{-1}$ [18]. On the contrary, in SnS the sizable difference between the band gap and the effective absorption threshold, which can be attributed to the indirect band gap, may cause a loss of efficiency. Furthermore, point defects in a Sn mixed-valence system have not been studied so far and are of great interest for defect physics.

In this study, we revisit the bulk properties of the tin sulfides using first-principles calculations with the generalized-gradient approximation (GGA) with a vdW correction [24–26], the Heyd-Scuseria-Ernzerhof hybrid functional (HSE06) [27–29], and the GW_0 approximation [30] and discuss their electronic structures, band-edge positions, and thermodynamical stability. We also show the calculated results of native point defects using the GGA with a vdW correction along with a GW_0 band-edge correction and examine the electronic properties and atomic structures of defects for each phase. For Sn_2S_3, we calculate the monovalent dopants in order to discuss the possibility of its *p*-type doping.

II. COMPUTATIONAL DETAILS

All calculations are performed using the projector augmented-wave (PAW) method [31] as implemented in VASP [32,33]. PAW data sets with radial cutoffs of 1.59 Å for Sn and 1.01 Å for S are employed. Sn 5*s* and 5*p* and S 3*s* and 3*p* are described as valence electrons. For the perfect crystals, lattice constants and internal atomic positions are fully optimized until the residual stresses and forces converge to less than 0.02 GPa and 0.005 eV/Å, respectively. Wave functions are expanded by a plane-wave basis set with 550-eV cutoff energy. Calculations with the GW_0 approximation [30,34,35] are conducted using a harder Sn PAW data set with a radial cutoff of 1.27 Å including 4*d* orbitals as valence electrons.

The formation energy of a point defect is calculated as [36–38]

$$E_f[D^q] = \{E[D^q] + E_{\mathrm{corr}}[D^q]\} - E_P - \sum n_i \mu_i + q(\epsilon_{\mathrm{VBM}} + \Delta\epsilon_F), \tag{1}$$

where $E[D^q]$ and E_P are the total energies of the supercell with defect D in charge state q and the perfect crystal supercell without any defect, respectively. n_i is the number of removed ($n_i < 0$) or added ($n_i > 0$) i-type atoms, and μ_i refers to the chemical potential. The chemical potentials can vary in the range that the host material considered is stable. ϵ_{VBM} is the energy level of the valence-band maximum (VBM), and $\Delta\epsilon_F$ represents the Fermi level with respect to the VBM. Apart from the approximation in the exchange-correlation functional, an error in the defect-formation energy mainly comes from the spurious electrostatic interactions between a defect cell and its images under the periodic boundary conditions, and $E_{\mathrm{corr}}[D^q]$ corresponds to an energy for correcting it. Here, we employ our extended Freysoldt–Neugebauer–Van de Walle (FNV) correction scheme [38,39] (see Appendix). In our scheme, we can account for the anisotropic screening of defect charges using dielectric tensors and treat systems with atomic relaxation by using the atomic-site local potential as a potential marker [38]. Note that the conventional potential alignment is unnecessary when the image-charge correction is properly applied to the defect-formation energy [38,40].

As discussed below, we perform the cell relaxation of perfect crystals with various exchange-correlation functionals: the local density approximation (LDA) [41], Perdew-Burke-Ernzerhof generalized-gradient approximation (PBE) [24], PBE with a vdW correction proposed by Grimme *et al.* with Becke-Jonson damping (PBE-D3) [25,26], and HSE06 [27–29] with (HSE06-D3) and without the vdW correction. We find that the lattice constants of the tin sulfides are best reproduced by PBE-D3 [25], and thus all defect calculations are performed with this level of theory. The band-edge positions are corrected based on the quasiparticle (QP) shifts obtained using GW_0 on top of PBE (GW_0@PBE) [30]. The Green's function is updated four times for convergence of the QP shifts.

The cutoff energy for the defect calculations is set to 280 eV, and spin polarization is considered for all defects except for those with Cu dopants, for which 300 eV is used for the calculations of supercells with and without a defect involved in Eq. (1). We emphasize that the spin polarization can reduce the energy of a defect with even-numbered electrons when a triplet is more stable than a singlet. The internal atomic positions are relaxed until the residual forces acting on all atoms are reduced to less than 0.03 eV/Å. The cell-size dependences of the defect-formation energies with and without the aforementioned size corrections are carefully checked with the defects having the largest absolute charge states in this study, which are expected to have the largest errors (see

Appendix). Finally, we adopt $5 \times 5 \times 2$ (containing 400 atoms before introducing a defect), $2 \times 5 \times 2$ (400 atoms), and $6 \times 6 \times 3$ (324 atoms) supercells for SnS, Sn_2S_3, and SnS_2, respectively, minimizing errors to less than 0.05 eV.

III. RESULTS AND DISCUSSION

A. Fundamental properties of the perfect crystals

Figure 1 presents the crystal structures of α-SnS ($Pnma$), Sn_2S_3($Pnma$), and 2H-SnS_2($P\bar{3}m1$), which are considered ground-state structures of the tin sulfides. It is noteworthy that every S ion is coordinated by three Sn in all the tin sulfides. However, the Sn─S bonds in SnS are 0.5 Å longer on average than those in SnS_2, reflecting the larger ionic radius of Sn(II) with a lone pair than that of Sn(IV). Sn(II) in SnS is coordinated by three S, and the lone pair points to the interlayer free space. SnS_2 also has a layered structure similar to other transition-metal dichalcogenides [42], in which Sn(IV) is octahedrally coordinated by six S. The unit cell of Sn_2S_3 is larger, contains 20 atoms, and is structurally a superposition of SnS and SnS_2: Half of Sn are coordinated by three S, whereas the other half are coordinated by six S. Indeed, the Bader charges [43,44] of two Sn sites in Sn_2S_3 are +1.0 and +1.5 when using PBE at the PBE-D3 equilibrium lattice constants, which are very close to those of SnS (+0.9) and SnS_2 (+1.5), respectively. The assigned Sn(II) and Sn(IV) are shown in Fig. 1(b).

Table I summarizes the calculated lattice constants of the tin sulfides using the LDA, PBE, HSE06, PBE-D3, and HSE06-D3 functionals along with experimental values. As typically found, the lattice constants are underestimated by LDA and overestimated by PBE in most cases [47]. Such tendencies are remarkable along the interlayer directions (the c directions for SnS and SnS_2 and the diagonal directions in the ac plane for Sn_2S_3). HSE06, which usually reproduces the experimental lattice constants satisfactorily, does not improve the interlayer distances. On the other hand, PBE-D3 gives the best accordance including the interlayer distances, meaning the inclusion of the vdW interactions plays an important role for the tin sulfides. Although HSE06-D3 outperforms HSE06 overall, all the lattice constants are underestimated to some extent. Vidal *et al.* report that the interlayer distance in SnS largely correlates to defect-formation energies [1], and, thus, PBE-D3 would be suited for defect calculations of the tin sulfides.

Table II shows the theoretical band gaps obtained using LDA, PBE, and HSE06 at their equilibrium lattice constants and those using PBE, HSE06, and GW_0@PBE at the PBE-D3 lattice constants [48]. The band-edge positions in the tin sulfides mostly lie on the lines between the special points in reciprocal space or even step out of the lines. As such, we calculate the band gaps by using a dense k-point sampling. Such calculations are, however, computationally too demanding when using GW_0. Therefore, we evaluate the GW_0 band gaps from a linear interpolation of QP shifts calculated at the k-point grids used for typical bulk calculations. This is justified by the fact that the k-vector dependence of the QP shifts is rather small in the tin sulfides as also mentioned by Vidal *et al.* for SnS [49].

The LDA gaps are significantly underestimated compared to the experimental gaps, whereas the PBE gaps are in closer agreement. HSE06 usually reproduces experimental band gaps quite successfully. However, it overestimates the gaps by a few tenths of eV or more at the HSE06 equilibrium lattice constants compared to the experimental gaps. When adopting the PBE-D3 lattice constants, the gaps are reproduced by HSE06 successfully, indicating that the band gaps of the tin sulfides strongly correlate to the lattice constants. This is

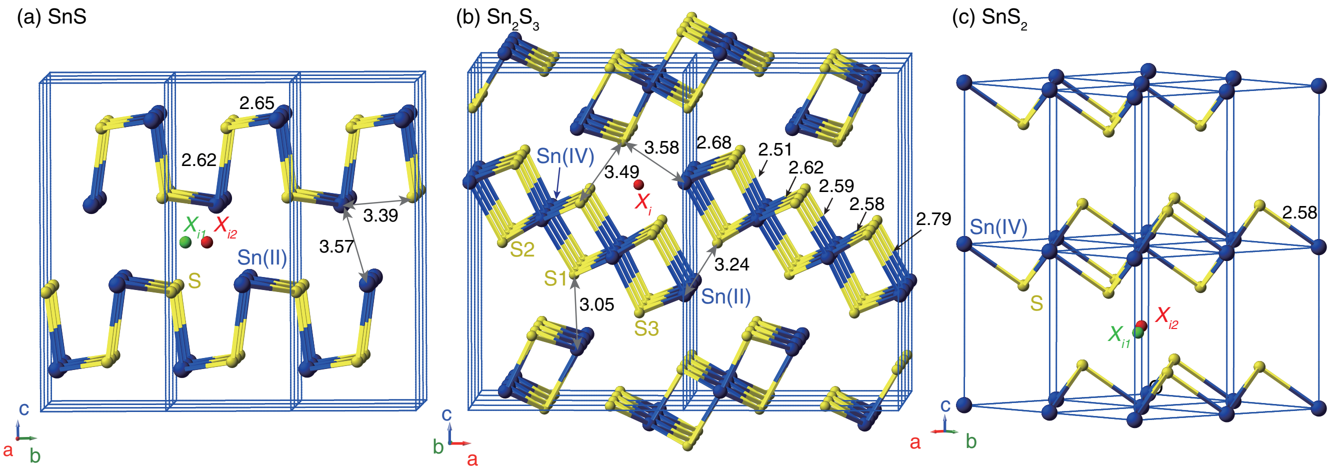

FIG. 1. Crystal structures of (a) SnS, (b) Sn_2S_3, and (c) SnS_2. The unit cells of SnS, Sn_2S_3, and SnS_2 contain 8, 20 and 3 atoms, respectively. Large blue balls represent the Sn atoms, whereas small yellow balls represent S atoms. Sn(II) and Sn(IV) are also distinguished in Sn_2S_3 based on the Bader charge analysis (see the text). The interstitial sites considered for the defect calculations are also depicted as X_{i1}, X_{i2}, and X_i. The bond distances in the PBE-D3 theoretical equilibrium structures are shown in angstroms.

TABLE I. Calculated lattice constants of the tin sulfides using several exchange-correlation functionals, along with experimental values [14,45,46] (in angstroms). Mean absolute percentage errors (MAPE) compared to experimental values are also shown.

	SnS			Sn_2S_3			SnS_2		
	a	b	c	a	b	c	a	c	MAPE
LDA	3.96	4.16	10.97	8.60	3.76	13.59	3.63	5.71	2.2
PBE	4.03	4.43	11.42	9.30	3.79	14.41	3.70	6.89	3.9
HSE06	3.96	4.45	11.32	9.21	3.74	14.55	3.65	6.81	3.3
PBE-D3	4.00	4.24	11.13	8.78	3.78	13.78	3.66	5.81	1.3
HSE06-D3	3.93	4.25	10.93	8.82	3.72	13.69	3.62	5.73	1.7
Experiments	3.97	4.34	11.14	8.87	3.75	14.02	3.65	5.90	⋯

TABLE II. Calculated band gaps of the tin sulfides using different exchange-correlation functionals in DFT and the GW_0@PBE approximation (in eV). Structures adopted for the calculations are also shown in the second row. All the experimental values are at room temperature. Note that SnS and SnS_2 are known to have indirect gaps, which are relatively difficult to determine from optical-absorption measurements.

	LDA	PBE	HSE06	PBE	HSE06	GW_0	Experiments
Structure	LDA	PBE	HSE06	PBE-D3			
SnS	0.44	0.89	1.29	0.62	0.98	0.92	1.08 [2]
Sn_2S_3	0.25	0.78	1.54	0.42	0.95	1.09	1.05 [18]
SnS_2	1.10	1.54	2.47	1.28	2.11	2.31	2.25 [14]

presumably because smaller lattice constants lead to larger band dispersions in the tin sulfides, which result in smaller band gaps. Consequently, such a gap lowering also occurs with PBE, but the LDA gaps increase when adopting the PBE-D3 lattice constants. GW_0@PBE reproduces the experimental gaps accurately at the PBE-D3 lattice constants. Therefore, we discuss the defect energetics using the GW_0@PBE-D3 band-edge positions in Sec. III C. We also find that spin-orbit coupling (SOC) only slightly lowers the gaps of SnS and SnS_2 by 0.02 and 0.05 eV and that of Sn_2S_3 by less than 0.01 eV when using PBE, and thus the SOC is ignored in this study.

Some researchers report much larger experimental band gaps for SnS (e.g., 1.3–1.7 [50] and 1.70 eV [51]) and Sn_2S_3 (e.g., 2 [52] and 1.9–2.2 eV [53]). These values seem unphysical, since the Sn lone-pair electrons are expected to reduce the band gaps of SnS and Sn_2S_3 from that of SnS_2 as can be inferred from the tin oxides (3.6 eV for SnO_2 [54] and 0.7 eV for SnO [55]). Contamination of SnS_2 [50] or alloying with oxygen might be a part of the reason. Thus, a cautious analysis of the chemical composition is required, especially for the less-studied Sn_2S_3.

The band structures and density of states of the tin sulfides obtained using HSE06 at the PBE-D3 theoretical lattice constants are shown in Fig. 2. As seen, the band-edge positions deviate from the special points in the reciprocal space, except for the conduction-band minimum (CBM) of Sn_2S_3. The band-edge positions are, however, not conclusive in our calculations, since more than one extremum is very close in energy at each band edge. The lone pairs of Sn-5sp comprise the VBM, with a bandwidth of about 2.5 eV for SnS and 1.5 eV for Sn_2S_3, whereas S-3p orbitals mainly construct that of SnS_2. On the other hand, the unoccupied Sn-5s bands locate at the CBM of Sn_2S_3 and SnS_2 with a bandwidth of about 1.5 eV for Sn_2S_3 and 2 eV for SnS_2, whereas Sn-5p orbitals mainly constitute that of SnS.

Slab calculations give us the band-edge positions with respect to the vacuum level and, thus, the relative positions between different solids. Figure 3(a) shows the calculated band-edge positions of the tin sulfides using PBE and GW_0@PBE at the PBE-D3 equilibrium lattice constants with and without atomic relaxations. The sign-reversed VBM positions with atomic relaxations correspond to the ionization potentials (IPs). Our calculated IP of the SnS at the (010) surface using GW_0@PBE (5.1 eV) is close to the value of 5.3 eV reported by Stevanović *et al.* using the same approximation [56].

The GW calculations change the VBM calculated by PBE rather than the CBM. We note that a similar tendency is also reported recently for various other compounds including sulfides [57–60]. The surface dipole depends on the surface orientation, and so does the band-edge position. Stevanović *et al.* show that the IP of SnS can change by up to 0.9 eV depending on the surface orientation [56]. Such a variation is remarkably large especially when comparing between Tasker type-1 and type-2 surfaces [61]. For example, the calculated IPs of

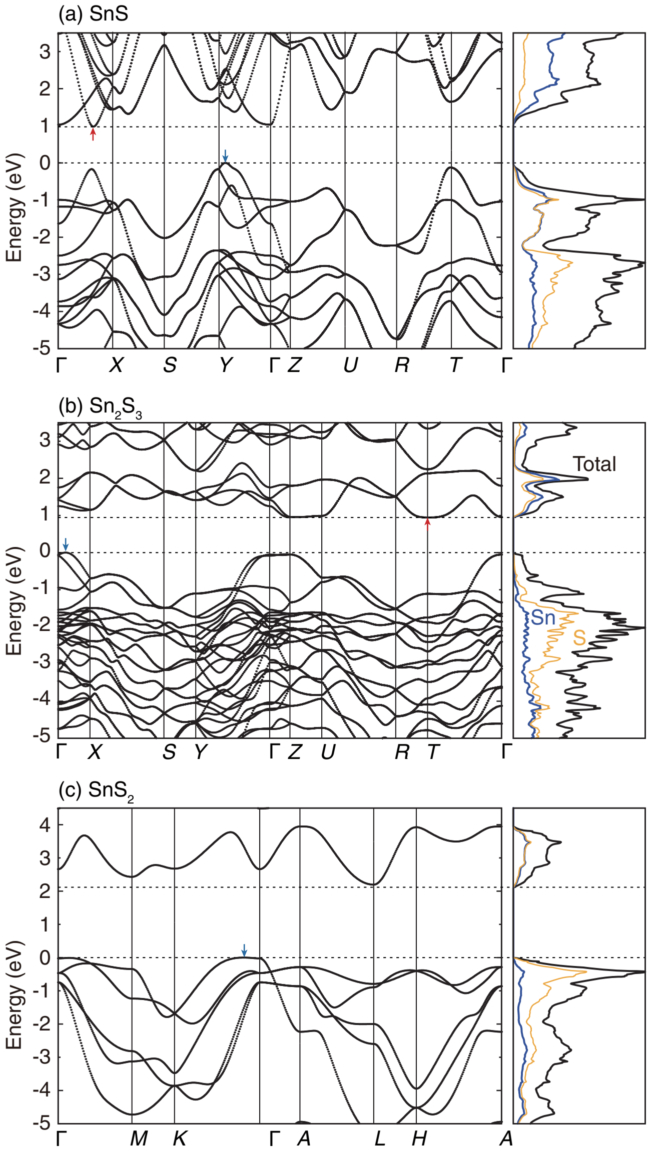

FIG. 2. Calculated band structures and density of states of (a) SnS, (b) Sn_2S_3, and (c) SnS_2 using HSE06 at the PBE-D3 equilibrium lattice constants. The energy zeros are set at the VBM. Horizontal dashed lines mean the VBM and CBM, and arrows indicate their positions in reciprocal space. Note that the CBM in SnS_2 does not appear in the band path shown.

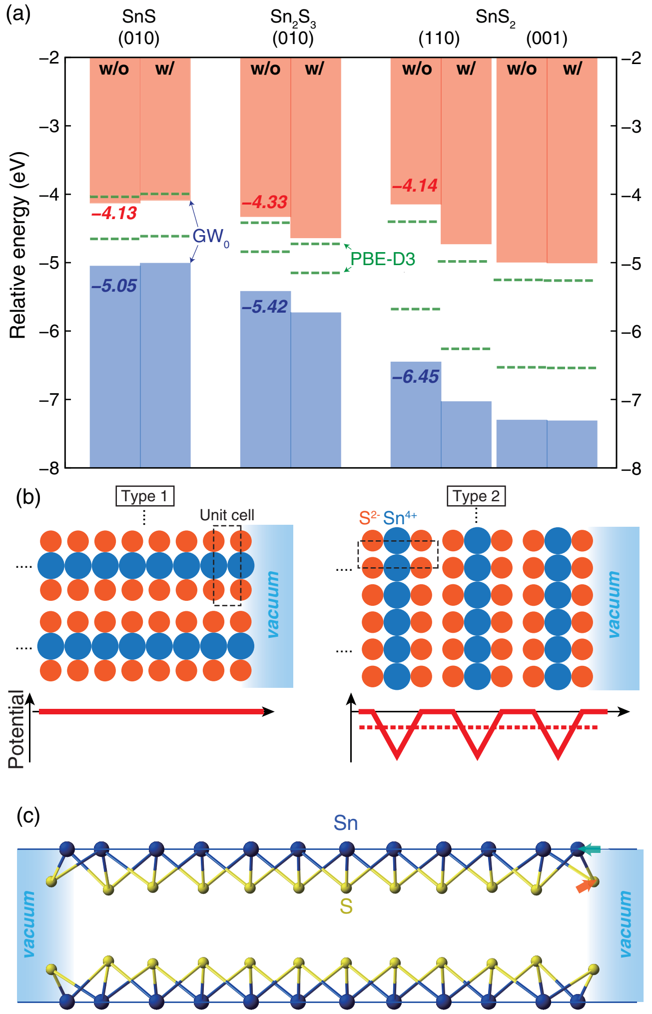

FIG. 3. (a) Band-edge positions of the tin sulfides with respect to the vacuum level calculated using PBE and GW_0@PBE at the PBE-D3 lattice constants. Both results with (w/) and without (w/o) atomic relaxation are shown. Note that the band-edge positions depend on the surface orientation. The (010) surfaces of SnS and Sn_2S_3 and (110) surface of SnS_2 are classified to Tasker type 1, whereas the (001) surface of SnS_2 is type 2 (see the text for details). (b) Schematic illustrations of the potential shift in SnS_2 for electrons induced by Tasker type-1 and type-2 surfaces. Point-charge models composed of hypothetical Sn^{4+} and S^{2-} ions are supposed for simplicity. The unit-cell-averaged potential is shown by a dashed line. (c) Relaxed (110) surface of SnS_2 using a slab model with a mirror symmetry. Tins move inward, whereas sulfurs move outward near the surface, which decreases the potential for electrons inside SnS_2.

rutile TiO_2 are 5.6 and 7.8 eV for (001) and (100) surfaces, which are categorized into Tasker type 1 and type 2, respectively [58]. As illustrated in Fig. 3(b), when anions exist on a surface exterior (Tasker type-2 surface), the potential for electrons is decreased inside a solid, which can explain why the band edges at the (001) surface in SnS_2 are lower than those at the (110) surface. Besides, when relaxing the (110) surface of SnS_2, the sulfurs move towards the surface, as shown in Fig. 3(c), and hence the band-edge positions drop after the relaxation. Thus, to avoid such surface-derived variations, band-edge positions calculated by Tasker type-1 surfaces without atomic relaxation are adopted for discussing the relative band-edge positions in this study.

The VBM of SnS_2 is 1.4 and 1.0 eV lower than those of SnS and Sn_2S_3, respectively. This tendency is probably due to the absence of the lone pairs in SnS_2 as shown above. On the other hand, the CBMs almost align in the tin sulfides. The VBM and CBM of Sn_2S_3 are slightly lower than those of SnS. The heterojunctions between *p*-SnS and *n*-Sn_2S_3

could be suitable for photovoltaics, since atomic diffusion and secondary phases at the interface would not pose serious problems due to the common constituents, and the band discontinuity, which is likely to make electric loss, would be fairly low. The only remaining potential issue is the lattice mismatch.

B. Formation energies

Figure 4 shows the convex hull of the Sn-S system at 0 K calculated using PBE, HSE06, PBE-D3, and PBE with empirical fitted element reference energies (PBE + FERE) [63], in which the energies of elements in their standard state phases are corrected so as to reproduce the experimental enthalpies of a wide variety of insulators and semiconductors. The energies of stable α-Sn ($Fd\bar{3}m$), SnS, Sn_2S_3, SnS_2, and α-S ($Fddd$) at 0 K are considered. The accuracy of the formation energies of host materials is important for defect calculations, since they directly relate to the defect-formation energies via atomic chemical potentials. PBE and HSE06 give lower formation energies compared to the experimental values, whereas PBE-D3 and PBE + FERE show good agreement. This tendency agrees with a previous report [64]. Therefore, PBE-D3 is also suited for defect calculations from this viewpoint.

The chemical potentials of Sn and S used for evaluating point-defect-formation energies are represented as A, B, and C in Fig. 4. Those in SnS can be varied in between A and B, whereas those in SnS_2 can be varied in between B and C. The energy of Sn_2S_3 lies almost on the line connecting the formation energies of SnS and SnS_2 denoted as B, reflecting the structural characteristics of their superposition. This means that the chemical potentials cannot be varied significantly in Sn_2S_3 by changing the growth condition. The stability of Sn_2S_3 could be, however, enhanced by temperature effects including phonon contributions to free energy.

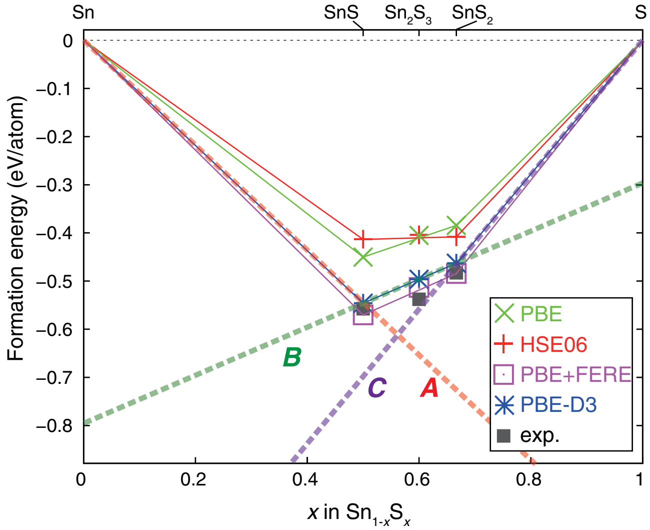

FIG. 4. The calculated formation energies of SnS, Sn_2S_3, and SnS_2 using PBE, HSE06, and PBE-D3 functionals and PBE with FERE corrections as well as those from the experiments at 298 K [62]. Three chemical potential conditions used for point-defect calculations, namely, (A) the Sn-rich condition for SnS, (B) the condition where the formation energies of SnS, Sn_2S_3, and SnS_2 lie on the tie line within less than 0.15 meV/atom, and (C) the S-rich condition for SnS_2, are shown.

C. Point defects

Here, we discuss the formation energies and thermodynamical transition levels of native point defects and atomic defect structures in the tin sulfides. In this study, we consider vacancies, antisites, and interstitials shown in Fig. 1 and cover a wide range of charge states for each defect. Only the result with the lowest energy is shown for each defect. We also discuss the ambipolar dopability of Sn_2S_3, which has great potential for photovoltaics and electronic devices. It should be emphasized that the defect-formation energies can generally include errors of a few tenths of eV even after the aforementioned cell-size corrections, which come mainly from the approximation to the treatment of the electron exchange-correlation interactions.

1. SnS

First, we revisit native point defects in SnS using PBE-D3. Vidal *et al.* calculate the point defects using PBE and correct the PBE band-edge positions using the GW_0@PBE approximation for evaluating defect-formation energies [1]. They adopt the experimental lattice constants, since the interlayer distance is found to considerably correlate to defect-formation energies. Malone, Gali, and Kaxiras calculate impurities as well as the native point defects using PBE [65]. They adopt the PBE theoretical lattice constants and extend the CBM by 0.35 eV so as to recover the experimental gap from the underestimated PBE gap. For correcting cell-size errors on defect energetics, Vidal *et al.* adopt the scheme proposed by Lany and Zunger along with the isotropic dielectric constant [49], whereas Malone, Gali, and Kaxiras use point-charge corrections in conjunction with an anisotropic dielectric tensor [66]. Since the former and the latter are devoid of a consideration of the anisotropy of the dielectric response [67] and the influence of a finite distribution of a defect charge density, respectively, our extended FNV scheme is superior to both these schemes. Their equivalent conclusions are (i) the fabrication of n-type SnS seems difficult without doping, and (ii) tin vacancies (V_{Sn}) are major acceptors, whereas sulfur vacancies (V_{S}) are major donors but have a deep donor level.

Figure 5 shows the energetics of native point defects in SnS at Sn-rich (S-poor) and Sn-poor (S-rich) chemical potential conditions. Our results are close to those of Malone, Gali, and Kaxiras rather than those of Vidal *et al.*, yet the band edges are deeper in energy so that n-type

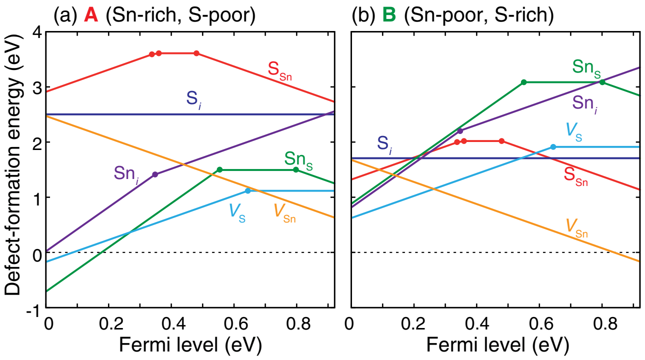

FIG. 5. Formation energies of native point defects in SnS as a function of the Fermi level under (a) Sn-rich (S-poor) and (b) Sn-poor (S-rich) chemical potential conditions. The Fermi level ranges from the valence-band maximum, which is set to zero, to the conduction-band minimum. V in defect species denote vacancies, and the subscripts denote defect sites, where i means interstitial sites. The charge states of defects correspond to the gradients. Only the most energetically favorable charge state at a given Fermi level is shown for each defect. Positive and negative charge states mean donor and acceptor behavior, respectively. The Fermi level at which the favorable charge state changes corresponds to the positions of donor or acceptor levels, which are designated by solid circles.

conversion is more plausible. This is because in our study the VBM is lowered by 0.52 eV and the CBM by 0.09 eV based on the GW_0@PBE calculation, which is in stark contrast with the upward shift of the CBM performed by Malone, Gali, and Kaxiras.

The major defects are V_{Sn} and V_{S}, whereas the tin and sulfur interstitials (Sn_i and S_i) have higher energies. Although the sulfur-on-tin antisites (S_{Sn}) have also higher energy in any condition, tin-on-sulfur antisites (Sn_{S}) can be major defects at Sn-rich conditions with a lower Fermi level. At the Sn-poor condition [Fig. 5(b)], SnS takes the p type, whereas at the Sn-rich condition [Fig. 5(a)], the n type might be attained. V_{S}, however, has a deep donor level, and hence it would be difficult to introduce a number of electron carriers without doping. This result is consistent with the experimental findings that undoped SnS shows p-type conductivity or high resistivity.

In experiments, p-type doping can be attained by Cu or Ag. For n-type conversion, on the other hand, aliovalent ion doping by Bi or Sb to a Sn site has not been successful to date. Ran *et al.* report that alloying Sn with Pb increases the interlayer spacing and lowers the energy of Sn_i, leading to n-type conversion at $x > 0.15$ in $\mathrm{Sn}_{1-x}\mathrm{Pb}_x\mathrm{S}$ [2]. As can be inferred from the calculations of Malone, Gali, and Kaxiras [65] combined with our GW_0 band-edge shifts, Cl doping at the Sn-rich condition might be an alternative candidate for n-type doping. Indeed, very recently, Yanagi *et al.* reported n-type SnS by Cl doping [68].

Figures 6(a)–6(d) shows the local structures near selected defects with lower formation energies in SnS. V_{Sn}^{-2} repels the neighboring S, simply because of ionic repulsion. In the case of V_{S}^{0}, neighboring Sn move inward with constructing a Sn-Sn deep localized state within the band gap. On the contrary, Sn near V_{S}^{+2} move outward, and the localized state locates over the CBM. This is typically found in anion vacancies including oxygen vacancy in ZnO [69]. We again perform the geometry optimization after adding two electrons (e^-) into V_{S}^{+2} and see if the perturbed host states remain, but $V_{\mathrm{S}}^{+2} + 2e^-$ eventually recovers to V_{S}^{0} with a deep localized state as shown in Fig. 6(b). Intriguingly, in the case of $\mathrm{Sn}_{\mathrm{S}}^{+4}$, Sn displaces to the interstitial site from V_{S} as shown in Fig. 6(d). Therefore, $\mathrm{Sn}_{\mathrm{S}}^{+4}$ can be regarded as a pair of V_{S} and Sn_i. Since $E_f(V_{\mathrm{S}}^{+2}) + E_f(\mathrm{Sn}_i^{+2})$ is 0.59 eV lower than $E_f(V_{\mathrm{S}}^{0}) + E_f(\mathrm{Sn}_i^{+4})$, $\mathrm{Sn}_{\mathrm{S}}^{+4}$ should be a pair of V_{S}^{+2} and Sn_i^{+2}. The binding energy, namely, $E_f(V_{\mathrm{S}}^{+2}) + E_f(\mathrm{Sn}_i^{+2}) - E_f(\mathrm{Sn}_{\mathrm{S}}^{+4})$, is 0.88 eV. Such a split of an antisite defect into a vacancy and an interstitial is often

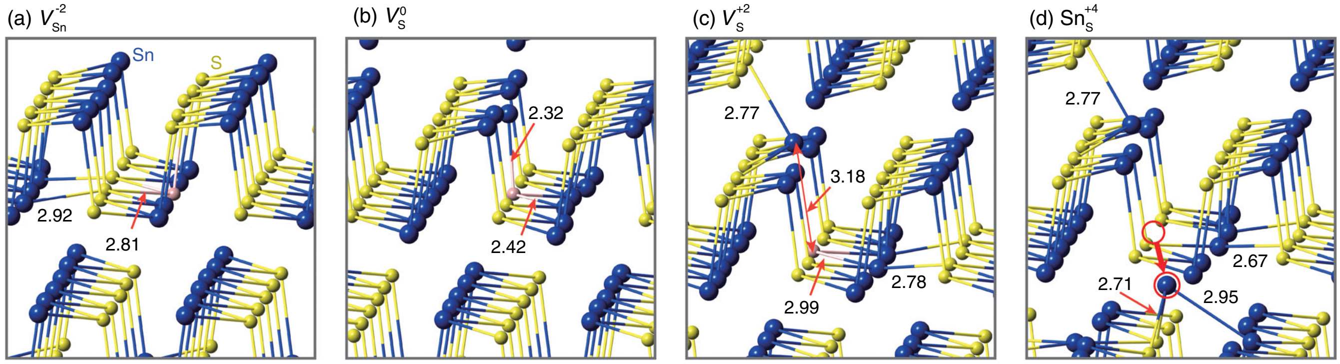

FIG. 6. Local structures of (a) V_{Sn}^{-2}, (b) V_{S}^{0}, (c) V_{S}^{+2}, and (d) $\mathrm{Sn}_{\mathrm{S}}^{+4}$ in SnS. Distances between an idealized vacancy position, which is assumed to be at the original position (pink balls), and neighboring defects are shown in angstroms. As a result of the large displacement of Sn at the S site, which is highlighted by red circles and a thick arrow, $\mathrm{Sn}_{\mathrm{S}}^{+4}$ can be regarded as a pair of V_{S}^{+2} and Sn_i^{+2} (see the text for details).

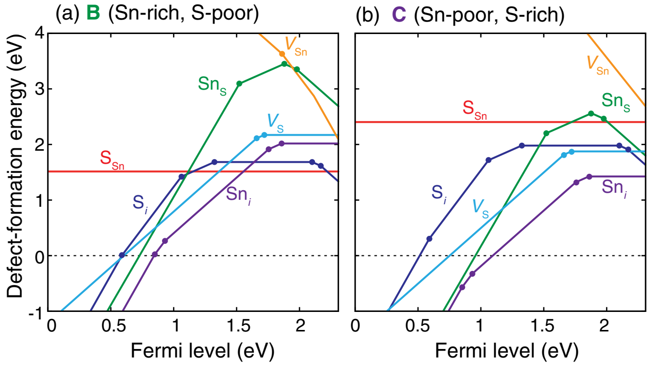

FIG. 7. Formation energies of native point defects in SnS_2 as a function of the Fermi level under (a) Sn-rich (S-poor) and (b) Sn-poor (S-rich) chemical potential conditions.

found in ionic compounds. However, it seems unusual that the positively charged defects have exothermic binding energy. This would be because of the size effect: SnS does have a small interlayer space, and, in consequence, Sn_i is likely to locate near a S vacancy. Indeed, Sn_i^{+2} involves significant local structural modification with a high formation energy.

2. SnS_2

Now, we discuss the point defects in SnS_2. Although SnS_2 has been intensively studied recent years, the calculations of defect properties have not been reported thus far. As in Fig. 7, our calculations predict n-type behavior of SnS_2 at entire growth conditions, which is consistent with the experimental report of n type [18–20]. All the defects except for V_{Sn} can be abundant depending on the growth condition and the Fermi level. It is worth noting that the defect-formation energies in SnS_2 form a contrast to those in SnS even at the same chemical potential condition B. For instance, V_{Sn} in SnS_2 has much higher energy than in SnS, presumably due to a variation in the coordination numbers of Sn (six in SnS_2 vs three in SnS). On the contrary, the interstitials have much lower energies, which can be attributed to a larger free space in between weakly bounded SnS_2 layers. In fact, the energies of the interstitials are lowered even in SnS when expanding the interlayer spacing by, e.g., isovalent doping with Pb [2,7]. The results shown in Fig. 7 indicate that the donor-type defects have negative formation energies when the Fermi level is lowered. In such a case, they emerge spontaneously with releasing carrier electrons, and, as a result, the Fermi level is forced up to a point at which the energies of all the donor states become zero. Since the position of such a Fermi-level pinning is so high from the VBM, p-type conversion of SnS_2 cannot be attained even by external p-type doping.

Figures 8(a)–8(d) show the local structures of selected defects in SnS_2. Although V_S^0 is not accompanied by large structural modification, the neighboring Sn construct a deep in-gap state, resulting in a deep donor level. Sn_i^0 locates at the middle of the free interlayer space, with symmetric coordination distances, whereas S_i^0 locates near a S with constructing a covalent bond. The distance between S_i^0 and a neighboring S is 2.00 Å, which is close to those in sulfur simple substances (e.g., 2.04 Å in α-sulfur). Note that such a S–S covalent bond also occurs in SnS but with a higher energy. In SnS_2, Sn_S^{+4} is again regarded as a pair of V_S and Sn_i. Since $E_f(V_S^{+2}) + E_f(Sn_i^{+2})$ is 1.60 eV lower than $E_f(V_S^0) + E_f(Sn_i^{+4})$, Sn_S^{+4} should be a pair of $V_S^{+2} + Sn_i^{+2}$. The binding energy is, however, only 0.03 eV, probably because the energy gain for reducing the local strain near Sn_i is not as large as in SnS due to the larger interlayer free space in SnS_2. On the other hand, S_{Sn}^{+2} rests on the original Sn site with a symmetric atomic configuration with slightly shorter distances to neighboring S (2.58 → 2.46 Å).

3. Sn_2S_3

Here, we discuss the point defects in Sn_2S_3. The notations in Fig. 1(b) are used to represent irreducible atomic positions in Sn_2S_3, namely, Sn(II), Sn(IV), S1, S2, and S3. Figure 9 shows the calculated defect-formation energies. Since the point where $E_f(Sn_i^{+2})$ and $E_f(V_{Sn(II)}^{-2})$ intersect is close to the CBM rather than the VBM,

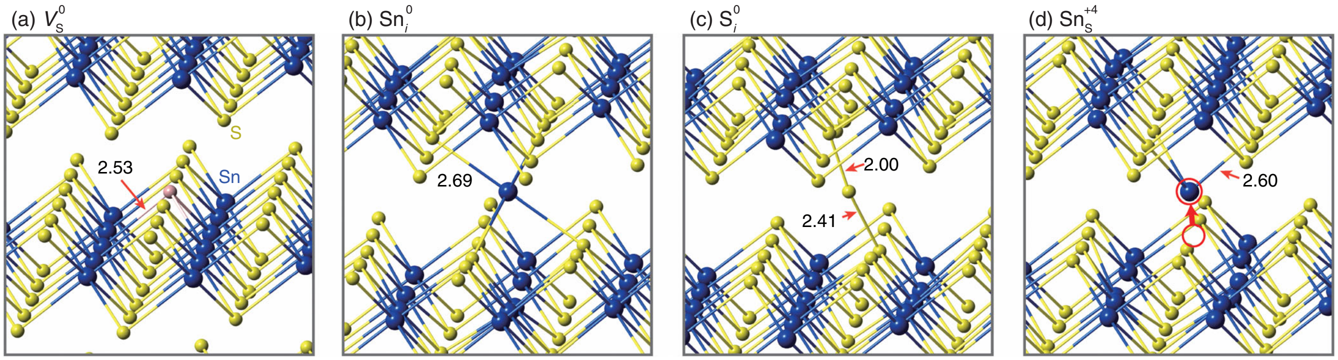

FIG. 8. Local structures of V_S^0, Sn_i^0, S_i^0, and Sn_S^{+4} in SnS_2. We note that Sn_S^{+4} can be regarded as a pair of V_S^{+2} and Sn_i^{+2} (see the text for details).

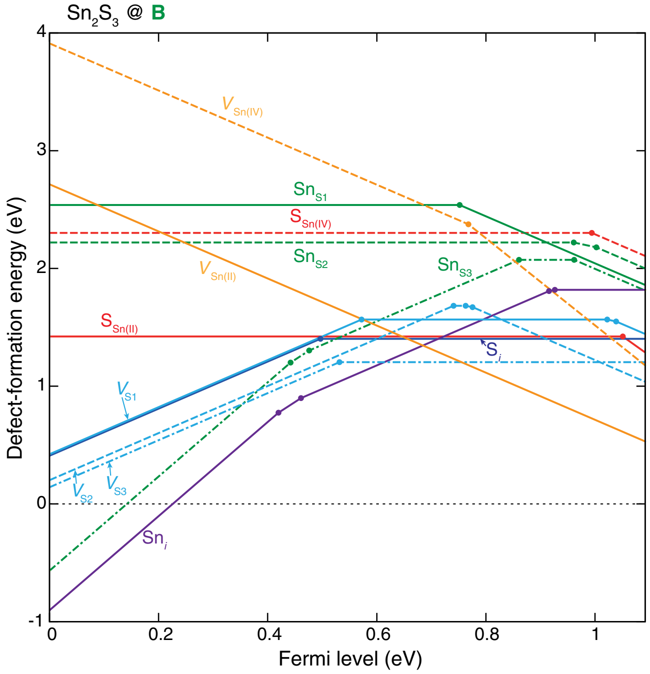

FIG. 9. Formation energies of native point defects in Sn_2S_3 as a function of the Fermi level at the chemical potential condition B in Fig. 4.

undoped Sn_2S_3 is expected to be n type, which is consistent with the experimental reports [18]. The other major defects are V_{S3}, S_i, and $S_{Sn(II)}$, but they are mainly in neutral charge states above the middle of the Fermi level and, thus, are inert with respect to carrier generation. As represented by the higher energy of $V_{Sn(IV)}$, the tendency of the defect-formation energies in Sn_2S_3 is generally understood from a combination of those in SnS and SnS_2. However, the formation energies of the tin vacancy and tin interstitial, which are the most stable acceptor and donor in Sn_2S_3, respectively, are not as low as those in SnS and SnS_2, respectively. These behaviors can be attributed to the differences in the band-edge positions and the size of interstitial sites. Therefore, they do not make deep Fermi-level pinning in Sn_2S_3 as shown in Fig. 9.

Figures 10(a)–10(d) show the local structures of V_{S2}^0, V_{S3}^0, Sn_i^{+2}, and S_i^0 in Sn_2S_3, respectively. Interestingly, the defect-formation energies and thermodynamical transition levels of V_{S1}, V_{S2}, and V_{S3} are different from each other as shown in Fig. 9, even though their coordination numbers are the same. In the case of V_{S2}^0, two Sn(IV) slightly move to the vacancy site, whereas a Sn(II) repels and constructs a chemical bond with another S with keeping the same coordination number. On the contrary, in the case of V_{S3}^0, two Sn(II) repel and make new bonds with the other S each. However, one Sn(IV) comes close to the vacancy site and has lone-pair electrons pointing to the vacancy site. Therefore, V_{S3}^0 can be represented as $V_{S3}^{+2} + \mathrm{Sn(II)}_{\mathrm{Sn(IV)}}$. The same situation occurs near V_{S1}^0 although it is higher in energy than V_{S3}^0, because S1 is coordinated by three Sn(IV) as in SnS_2, in which V_S has a higher formation energy. Sn_i and S_i show almost the same tendencies as in SnS_2; Sn_i locates in the middle of the interlayer space with a symmetric coordination environment, whereas S_i makes a covalent bond with another S.

4. Overall discussion of native defects in the tin sulfides

Here, we discuss the native defects in the tin sulfides overall.

Vacancies.—$V_{Sn(II)}$ are lower in energy compared to $V_{Sn(IV)}$. Consequently, $V_{Sn(II)}$ become a main source of native p-type conductivity in SnS and counteract carrier electrons in n-type Sn_2S_3, whereas $V_{Sn(IV)}$ are not abundant in Sn_2S_3 and SnS_2 and do not significantly affect the electronic conductivity. Their energy difference can be mainly attributed to the variation in the coordination numbers [three of Sn(II) vs six of Sn(IV)], since the vacancy formation energy generally increases with increasing the coordination number. On the other hand, although V_S have rather low energies especially in SnS and Sn_2S_3, they have deep donor levels.

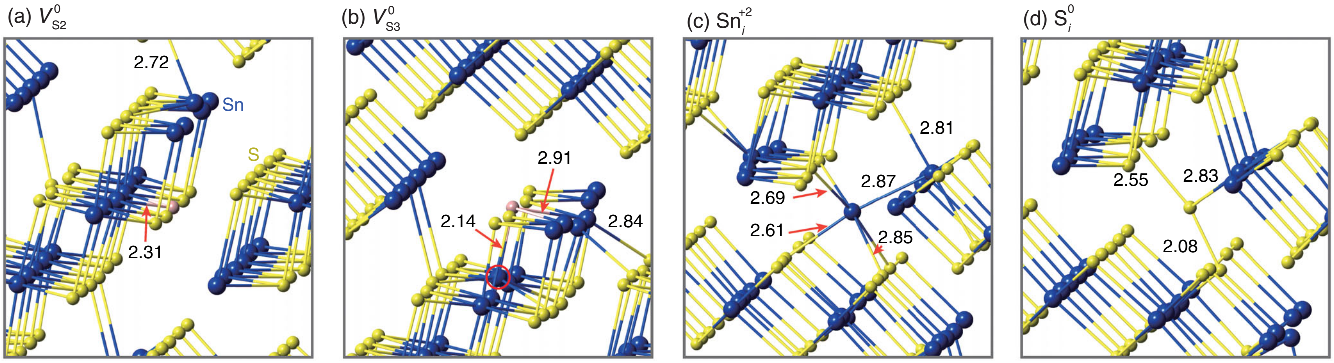

FIG. 10. Local structures of V_{S2}^0, V_{S3}^0, Sn_i^{+2}, and S_i^0 in Sn_2S_3. The Sn changing the oxidation state from +4 to +2 near an S3 vacancy is highlighted by a red circle.

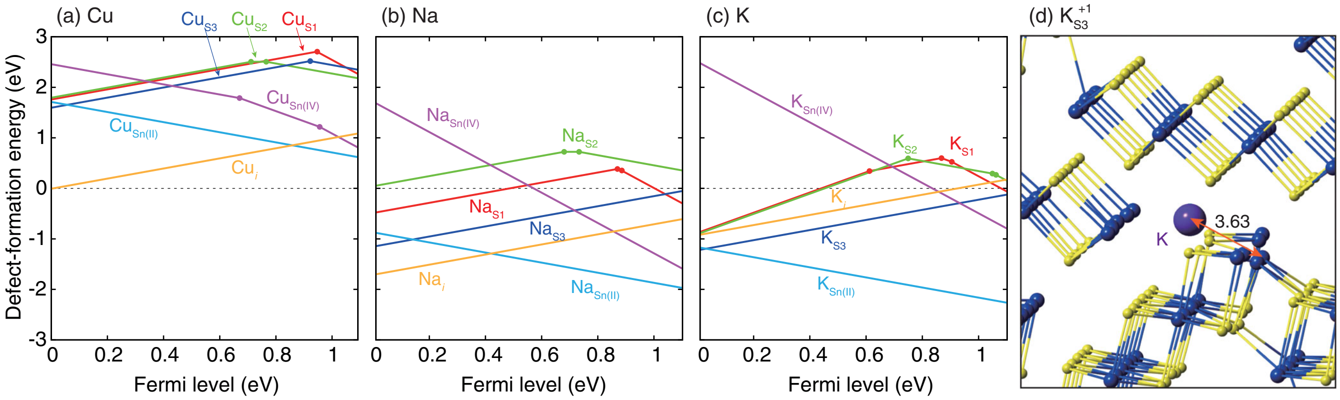

FIG. 11. Formation energies of (a) Cu, (b) Na, and (c) K dopants in Sn_2S_3 as a function of the Fermi level at the chemical potential condition B in Fig. 4. The chemical potentials of the dopants are fixed to the energies of their simple substances (see the text for details). (d) A local structure of K_{S3}^{+1} in Sn_2S_3.

Interstitials.—The formation energy of an interstitial strongly correlates to the size of the interlayer free space in the tin sulfides and, thus, decreases from SnS to Sn_2S_3 to SnS_2. Sn_i is likely to locate at the center of the free space, whereas S_i prefers to make a covalent bonding with a neighboring S with keeping the S—S distance close to that in α-sulfur. Sn_i acts as a deep donor in Sn_2S_3 and SnS_2 but a shallow donor in SnS. Therefore, n-SnS can be attained when the energy of Sn_i is decreased by increasing the interlayer free space via, e.g., alloying with PbS [2,7]. On the contrary, S_i are amphoteric with very deep donor and acceptor levels in all the tin sulfides.

Antisites.—The formation energy of an antisite strongly depends on the chemical potential condition, since the chemical potentials of two species are involved in the formation energy. The antisites do not play important roles in the tin sulfides in most cases compared to vacancies and interstitials due to their higher formation energies. In all the tin sulfides, Sn_S with a lower energy largely moves from the original S site to free space nearby. Therefore, Sn_S can be regarded as a combination of Sn_i and V_S. The exothermic binding energy between Sn_i and V_S increases as the interlayer space is decreased. On the other hand, S_{Sn} is likely to locate at the original Sn site with a higher energy and very deep donor and/or acceptor levels.

5. *p-type doping in* Sn_2S_3

As discussed in Sec. III C 3, the major carriers in undoped Sn_2S_3 are electrons. In contrast to SnS_2, however, p-type conversion might be plausible with external doping, since the Fermi-level pinning caused by Sn_i occurs at just 0.23 eV above the VBM (see Fig. 9). At this Fermi level, the hole carrier density at room temperature estimated from the density of states shown in Fig. 2(b) is 3×10^{15} cm^{-3}. The substitution of Sn with cations having fewer oxidation states may introduce holes, and hence monovalent elements would be suited since their oxidation states are lower than those of both Sn(II) and Sn(IV). However, cations locating at the interstitial sites, which generally counteract holes or even introduce carrier electrons, can be easily formed in the tin sulfides. Therefore, monovalent atoms with large ionic radii would be suited for p-type doping in Sn_2S_3. Here, we test this hypothesis through calculations of Cu, Na, and K dopants in Sn_2S_3.

The calculated results are shown in Figs. 11(a)–11(c). Note that the ionic radii increase from Cu (0.74 Å for 1 + oxidation state with 4-coordination) to Na (1.13 Å) to K (1.51 Å) [70]. It may be plausible to dope more impurities than their equilibrium concentrations when quenching materials or using nonequilibrium techniques such as ion implantation. Therefore, in this study, we discuss the relative formation energies of dopants. The chemical potentials of the dopants are fixed to the energies of their simple substances, and the possibility of secondary phases composed of the dopant and Sn and/or S is excluded.

As we expect, Cu, which has the smallest ionic radius among the dopants considered, is likely to locate at the interstitial site. Since the intersection point of $E_f(\mathrm{Cu}_i^{+1})$ and $E_f(\mathrm{Cu}_{\mathrm{Sn(II)}}^{-1})$ is near the CBM, Cu doping releases electron carriers. In the case of Na, the substitutional Na are more likely than interstitial ones when the Fermi level locates at the middle of the band gap or higher, and, as we expect, this tendency is more pronounced when doping K. As a result, $E_f(\mathrm{K}_{\mathrm{S3}}^{+1})$ and $E_f(\mathrm{K}_{\mathrm{Sn(II)}}^{-1})$ intersect just above the VBM, indicating that the K doping allows us to make p-Sn_2S_3.

Interestingly, K_{S3}^{+1} has a significantly lower formation energy even compared with K_i^{+1}. As shown in Fig. 11(d) illustrating the local structure of K_{S3}^{+1}, the K ion moves from the original S site to free space nearby as Sn_S antisites do. This is presumably because a K preferentially couples with a S vacancy so as to reduce the local strain caused by a large K.

IV. CONCLUSIONS

We revisit the lattice constants, electronic structures, and band alignments of the tin sulfides using the PBE + D3 functional and GW_0@PBE approximation. It is found that consideration of vdW interactions is important for reproducing the lattice constants of the tin sulfides, especially along the interlayer directions. Based on the Bader charge analysis, half of Sn in $\mathrm{Sn_2S_3}$ are assigned to Sn(II) and the other half to Sn(IV), which is also consistent with their local coordination environments. Regarding the band gaps, GW_0@PBE at the PBE-D3 lattice constants shows good agreement with experimental values. The VBM position lowers from SnS to $\mathrm{Sn_2S_3}$ to $\mathrm{SnS_2}$, whereas the CBM does not change significantly. We also calculate the convex hull of the Sn-S system and find that PBE-D3 can reproduce the experimental formation energies quite well. As a result, $\mathrm{Sn_2S_3}$ is found not to be very stable with respect to SnS and $\mathrm{SnS_2}$. This, however, seems natural, since its structural feature is described by a superposition of those of SnS and $\mathrm{SnS_2}$.

In the latter part of this paper, we systematically investigate the native point defects in the tin sulfides, i.e., vacancies, interstitials, and antisites using the PBE + D3 functional and the band-edge shift calculated by the GW_0@PBE approximation. In addition, we calculate the properties of monovalent dopants (Cu, Na, and K) in $\mathrm{Sn_2S_3}$ to introduce a guide for achieving p-type $\mathrm{Sn_2S_3}$. The spurious electrostatic errors in the defect-formation energies caused by the supercell modeling are removed using our extended FNV scheme. The native SnS is found to be p type or n type with a low carrier concentration depending on the growth conditions. The major defects in SnS are V_{Sn} and V_{S}, which are a shallow acceptor and a deep donor, respectively. $\mathrm{SnS_2}$ is found to be n type primarily due to Sn_i, which have a lower formation energy than in SnS. $\mathrm{SnS_2}$ is difficult to be inverted to p type even by external doping because of the deep Fermi-level pinning of Sn_i. The dominant point defects in $\mathrm{Sn_2S_3}$ are $V_{\mathrm{Sn(II)}}$, Sn_i, and V_{S}, which are a shallow acceptor, a shallow donor, and a deep donor, respectively. The calculated undoped $\mathrm{Sn_2S_3}$ is n type that is consistent with the experimental findings. To make p-$\mathrm{Sn_2S_3}$, we propose to dope with K because of its large ionic radius, which is a necessity to prevent the incorporation of dopants into the interstitial sites.

ACKNOWLEDGMENTS

This work was supported by the MEXT Elements Strategy Initiative to Form Core Research Center, Grants-in-Aid for Young Scientists A (Grant No. 15H05541), Scientific Research B (Grant No. 15H04125), and JSPS Fellows (Grant No. 26-04792) from JSPS. Computing resources of ACCMS at Kyoto University are used in this work.

APPENDIX: ENERGY CORRECTIONS FOR POINT DEFECTS

We here focus on errors in the defect-formation energies caused by the finite sizes of supercells and how accurately they are corrected using *a posteriori* electrostatics-based corrections. More details are discussed in Ref. [38]. In Fig. 12, the relative formation energies of $\mathrm{Sn_S^{+4}}$ in SnS, $V_{\mathrm{Sn(IV)}}^{-4}$ in $\mathrm{Sn_2S_3}$, and $V_{\mathrm{Sn(IV)}}^{-4}$ in $\mathrm{SnS_2}$ are shown as functions of supercell sizes. These defects have the largest absolute charge states in this study, which are likely to have the largest error in each system. When compared with similar-size supercells, the absolute error increases from SnS to $\mathrm{Sn_2S_3}$ to $\mathrm{SnS_2}$, because the error is roughly proportional to the reciprocal of a dielectric constant (see Table III) when the supercell size is the same. Note that the ionic contribution to the dielectric constant of $\mathrm{SnS_2}$

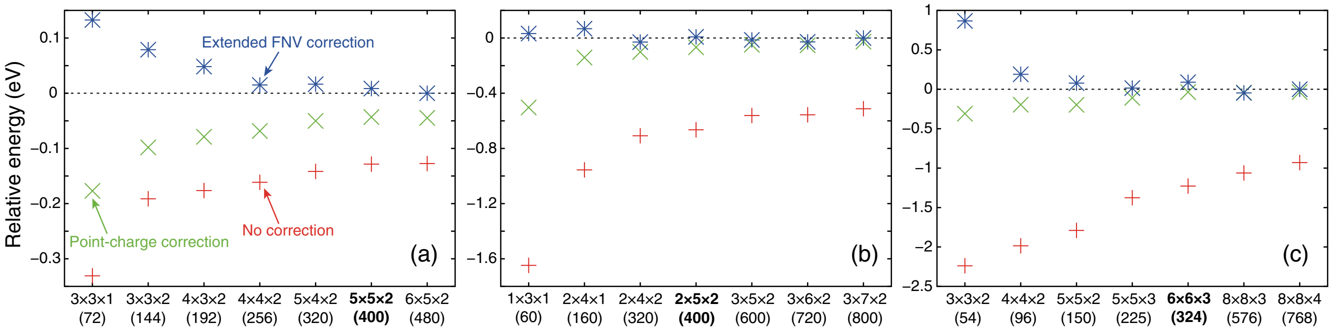

FIG. 12. Uncorrected, point-charge-corrected, and extended FNV-corrected relative defect-formation energies of (a) $\mathrm{Sn_S^{+4}}$ in SnS, (b) $V_{\mathrm{Sn(IV)}}^{-4}$ in $\mathrm{Sn_2S_3}$, and (c) V_{Sn}^{-4} in $\mathrm{SnS_2}$ as functions of supercell sizes. Zeros of the relative energies are set to the FNV-corrected energies with the largest supercells. The values in parentheses are the numbers of atoms in the supercells before introducing a defect. Supercell sizes in boldface type are used for the defect calculations in this study. Calculations are performed using PBE-D3 at its theoretical lattice constants.

TABLE III. Calculated ion-clamped dielectric tensors (ϵ^{ele}) and ionic contributions (ϵ^{ion}) of SnS, Sn_2S_3, and SnS_2 using PBE at the PBE-D3 theoretical lattice constants.

	SnS			Sn_2S_3			SnS_2	
	ϵ_{11}	ϵ_{22}	ϵ_{33}	ϵ_{11}	ϵ_{22}	ϵ_{33}	ϵ_{11}	ϵ_{33}
ϵ^{ele}	19.8	16.8	16.5	11.5	11.4	12.1	8.5	6.7
ϵ^{ion}	40.4	21.7	19.2	9.67	15.5	15.4	10.3	0.6

along the out-of-plane direction is relatively small, indicating SnS_2 holds more two-dimensional characteristics than the others.

We also show the relative defect-formation energies with point-charge corrections and extended FNV corrections in Fig. 12. In order to consider the anisotropic features, dielectric tensors are utilized for evaluating the point-charge potential and energies in both cases [38]. These corrections drastically improve the defect-formation energies. The FNV corrections take into account the finite defect-size effect and, hence, are usually superior to the point-charge ones. This is, however, not true when adopting smaller supercells as seen in SnS_2, because the other errors not considered in the extended FNV correction scheme may cancel out the difference fortuitously. Therefore, it is better to choose supercells with small errors after applying the FNV corrections. Based on the test calculations, we adopt $5 \times 5 \times 2$, $2 \times 5 \times 2$, and $6 \times 6 \times 3$ supercells for SnS, Sn_2S_3, and SnS_2, respectively, which allow us to estimate the defect-formation energies within an error of 0.05 eV.

[1] J. Vidal, S. Lany, M. d'Avezac, A. Zunger, A. Zakutayev, J. Francis, and J. Tate, Band-structure, optical properties, and defect physics of the photovoltaic semiconductor SnS, Appl. Phys. Lett. **100**, 032104 (2012).

[2] F.-Y. Ran, Z. Xiao, Y. Toda, H. Hiramatsu, H. Hosono, and T. Kamiya, n-type conversion of SnS by isovalent ion substitution: Geometrical doping as a new doping route, Sci. Rep. **5**, 10428 (2015).

[3] P. Sinsermsuksakul, L. Sun, S. W. Lee, H. H. Park, S. B. Kim, C. Yang, and R. G. Gordon, Overcoming efficiency limitations of SnS-based solar cells, Adv. Energy Mater. **4**, 1400496 (2014).

[4] A. Schneikart, H.-J. Schimper, A. Klein, and W. Jaegermann, Efficiency limitations of thermally evaporated thin-film SnS solar cells, J. Phys. D **46**, 305109 (2013).

[5] J. J. Loferski, Theoretical considerations governing the choice of the optimum semiconductor for photovoltaic solar energy conversion, J. Appl. Phys. **27**, 777 (1956).

[6] L. Sun, R. Haight, P. Sinsermsuksakul, S. B. Kim, H. H. Park, and R. G. Gordon, Band alignment of SnS/Zn(O, S) heterojunctions in SnS thin film solar cells, Appl. Phys. Lett. **103**, 181904 (2013).

[7] Z. Xiao, F.-Y. Ran, H. Hosono, and T. Kamiya, Route to n-type doping in SnS, Appl. Phys. Lett. **106**, 152103 (2015).

[8] P. Sinsermsuksakul, R. Chakraborty, S. B. Kim, S. M. Heald, T. Buonassisi, and R. G. Gordon, Antimony-doped tin(II) sulfide thin films, Chem. Mater. **24**, 4556 (2012).

[9] C. Bera, S. Jacob, I. Opahle, N. S. H. Gunda, R. Chmielowski, G. Dennler, and G. K. H. Madsen, Integrated computational materials discovery of silver doped tin sulfide as a thermoelectric material, Phys. Chem. Chem. Phys. **16**, 19894 (2014).

[10] S. Bhattacharya, N. S. H. Gunda, R. Stern, S. Jacobs, R. Chmielowski, G. Dennler, and G. K. H. Madsen, Achieving optimum carrier concentrations in p-doped SnS thermoelectrics, Phys. Chem. Chem. Phys. **17**, 9161 (2015).

[11] A. S. Rodin, L. C. Gomes, A. Carvalho, and A. H. Castro Neto, Valley physics in tin (II) sulfide, Phys. Rev. B **93**, 045431 (2016).

[12] T.-J. Kim, C. Kim, D. Son, M. Choi, and B. Park, Novel SnS_2-nanosheet anodes for lithium-ion batteries, J. Power Sources **167**, 529 (2007).

[13] J. w. Seo, J. t. Jang, S. w. Park, C. Kim, B. Park, and J. Cheon, Two-dimensional SnS_2 nanoplates with extraordinary high discharge capacity for lithium ion batteries, Adv. Mater. **20**, 4269 (2008).

[14] L. A. Burton, T. J. Whittles, D. Hesp, W. M. Linhart, J. M. Skelton, B. Hou, R. F. Webster, G. O'Dowd, C. Reece, D. Cherns, D. J. Fermin, T. D. Veal, V. R. Dhanak, and A. Walsh, Electronic and optical properties of single crystal SnS_2: An earth-abundant disulfide photocatalyst, J. Mater. Chem. A **4**, 1312 (2016).

[15] W. Shi, L. Huo, H. Wang, H. Zhang, J. Yang, and P. Wei, Hydrothermal growth and gas sensing property of flower-shaped SnS_2 nanostructures, Nanotechnology **17**, 2918 (2006).

[16] H. Zhong, G. Yang, H. Song, Q. Liao, H. Cui, P. Shen, and C.-X. Wang, Vertically aligned graphene-like SnS_2 ultrathin nanosheet arrays: Excellent energy storage, catalysis, photoconduction, and field-emitting performances, J. Phys. Chem. C **116**, 9319 (2012).

[17] H. S. Song, S. L. Li, L. Gao, Y. Xu, K. Ueno, J. Tang, Y. B. Cheng, and K. Tsukagoshi, High-performance top-gated monolayer SnS_2 field-effect transistors and their integrated logic circuits, Nanoscale **5**, 9666 (2013).

[18] A. Sanchez-Juarez and A. Ortíz, Effects of precursor concentration on the optical and electrical properties of Sn_XS_Y thin films prepared by plasma-enhanced chemical vapour deposition, Semicond. Sci. Technol. **17**, 931 (2002).

[19] G. Domingo, R. S. Itoga, and C. R. Kannewurf, Fundamental Optical Absorption in SnS_2 and $SnSe_2$, Phys. Rev. **143**, 536 (1966).

[20] K. Kourtakis, J. DiCarlo, R. Kershaw, K. Dwight, and A. Wold, Preparation and characterization of SnS_2, J. Solid State Chem. **76**, 186 (1988).

[21] M. Manikandan, T. Tanabe, P. Li, S. Ueda, G. V. Ramesh, R. Kodiyath, J. Wang, T. Hara, A. Dakshanamoorthy, S. Ishihara, K. Ariga, J. Ye, N. Umezawa, and H. Abe, Photocatalytic water splitting under visible light by mixed-valence Sn_3O_4, ACS Appl. Mater. Interfaces **6**, 3790 (2014).

[22] C. M. Caskey, A. Holder, S. Shulda, S. T. Christensen, D. Diercks, C. P. Schwartz, D. Biagioni, D. Nordlund, A. Kukliansky, A. Natan, D. Prendergast, B. Orvananos, W. Sun, X. Zhang, G. Ceder, D. S. Ginley, W. Tumas, J. D. Perkins, V. Stevanović, S. Pylypenko, S. Lany, R. M. Richards, and A. Zakutayev, Synthesis of a mixed-valent tin nitride and considerations of its possible crystal structures, J. Chem. Phys. **144**, 144201 (2016).

[23] V. Steinmann, R. Jaramillo, K. Hartman, R. Chakraborty, R. E. Brandt, J. R. Poindexter, Y. S. Lee, L. Sun, A. Polizzotti, H. H. Park, R. G. Gordon, and T. Buonassisi, 3.88% efficient tin sulfide solar cells using congruent thermal evaporation, Adv. Mater. **26**, 7488 (2014).

[24] J. P. Perdew, K. Burke, and M. Ernzerhof, Generalized Gradient Approximation Made Simple, Phys. Rev. Lett. **77**, 3865 (1996).

[25] S. Grimme, J. Antony, S. Ehrlich, and H. Krieg, A consistent and accurate *ab initio* parametrization of density functional dispersion correction (DFT-D) for the 94 elements H-Pu, J. Chem. Phys. **132**, 154104 (2010).

[26] S. Grimme, S. Ehrlich, and L. Goerigk, Effect of the damping function in dispersion corrected density functional theory, J. Comput. Chem. **32**, 1456 (2011).

[27] J. Heyd, G. E. Scuseria, and M. Ernzerhof, Hybrid functionals based on a screened Coulomb potential, J. Chem. Phys. **118**, 8207 (2003).

[28] J. Heyd, G. E. Scuseria, and M. Ernzerhof, Erratum: Hybrid functionals based on a screened Coulomb potential, J. Chem. Phys. **124**, 219906 (2006).

[29] A. V. Krukau, O. A. Vydrov, A. F. Izmaylov, and G. E. Scuseria, Influence of the exchange screening parameter on the performance of screened hybrid functionals, J. Chem. Phys. **125**, 224106 (2006).

[30] L. Hedin, New method for calculating the one-particle green's function with application to the electron-gas problem, Phys. Rev. **139**, A796 (1965).

[31] P. E. Blöchl, Projector augmented-wave method, Phys. Rev. B **50**, 17953 (1994).

[32] G. Kresse and J. Furthmüller, Efficient iterative schemes for *ab initio* total-energy calculations using a plane-wave basis set, Phys. Rev. B **54**, 11169 (1996).

[33] G. Kresse and D. Joubert, From ultrasoft pseudopotentials to the projector augmented-wave method, Phys. Rev. B **59**, 1758 (1999).

[34] M. S. Hybertsen and S. G. Louie, Electron correlation in semiconductors and insulators: Band gaps and quasiparticle energies, Phys. Rev. B **34**, 5390 (1986).

[35] M. Shishkin, M. Marsman, and G. Kresse, Accurate Quasiparticle Spectra from Self-Consistent *GW* Calculations with Vertex Corrections, Phys. Rev. Lett. **99**, 246403 (2007).

[36] S. B. Zhang and J. E. Northrup, Chemical Potential Dependence of Defect Formation Energies in GaAs: Application to Ga Self-Diffusion, Phys. Rev. Lett. **67**, 2339 (1991).

[37] C. Freysoldt, B. Grabowski, T. Hickel, J. Neugebauer, G. Kresse, A. Janotti, and C. G. Van de Walle, First-principles calculations for point defects in solids, Rev. Mod. Phys. **86**, 253 (2014).

[38] Y. Kumagai and F. Oba, Electrostatics-based finite-size corrections for first-principles point defect calculations, Phys. Rev. B **89**, 195205 (2014).

[39] C. Freysoldt, J. Neugebauer, and C. G. Van de Walle, Fully *Ab Initio* Finite-Size Corrections for Charged-Defect Supercell Calculations, Phys. Rev. Lett. **102**, 016402 (2009).

[40] Y. Kumagai, M. Choi, Y. Nose, and F. Oba, First-principles study of point defects in chalcopyrite $ZnSnP_2$, Phys. Rev. B **90**, 125202 (2014).

[41] J. P. Perdew and A. Zunger, Self-interaction correction to density-functional approximations for many-electron systems, Phys. Rev. B **23**, 5048 (1981).

[42] M. Chhowalla, H. S. Shin, G. Eda, L.-J. Li, K. P. Loh, and H. Zhang, The chemistry of two-dimensional layered transition metal dichalcogenide nanosheets, Nat. Chem. **5**, 263 (2013).

[43] R. F. W. Bader, *Atoms in Molecules: A Quantum Theory* (Oxford University, New York, 1990).

[44] W. Tang, E. Sanville, and G. Henkelman, A grid-based Bader analysis algorithm without lattice bias, J. Phys. Condens. Matter **21**, 084204 (2009).

[45] T. Chattopadhyay, J. Pannetier, and H. G. Von Schnering, Neutron diffraction study of the structural phase transition in SnS and SnSe, J. Phys. Chem. Solids **47**, 879 (1986).

[46] M. Cruz, J. Morales, J. P. Espinos, and J. Sanz, XRD, XPS and Sn NMR study of tin sulfides obtained by using chemical vapor transport methods, J. Solid State Chem. **175**, 359 (2003).

[47] We also calculate the lattice constants using harder PAW potentials with Sn-*d* electrons and find that the lattice constants are changed only within 0.3%.

[48] Note that the vdW correction proposed by Grimme *et al.* [25,26] changes the energy landscape of atomic configuration only and does not influence the electronic structures.

[49] S. Lany and A. Zunger, Assessment of correction methods for the band-gap problem and for finite-size effects in supercell defect calculations: Case studies for ZnO and GaAs, Phys. Rev. B **78**, 235104 (2008).

[50] O. E. Ogah, G. Zoppi, I. Forbes, and R. Miles, Thin films of tin sulphide for use in thin film solar cell devices, Thin Solid Films **517**, 2485 (2009).

[51] M. Calixto-Rodriguez, H. Martinez, A. Sanchez-Juarez, J. Campos-Alvarez, A. Tiburcio-Silver, and M. Calixto, Structural, optical, and electrical properties of tin sulfide thin films grown by spray pyrolysis, Thin Solid Films **517**, 2497 (2009).

[52] M. Khadraoui, N. Benramdane, C. Mathieu, A. Bouzidi, R. Miloua, Z. Kebbab, K. Sahraoui, and R. Desfeux, Optical and electrical properties of thin films grown by spray pyrolysis, Solid State Commun. **150**, 297 (2010).

[53] H. B. H. Salah, H. Bouzouita, and B. Rezig, Preparation and characterization of tin sulphide thin films by a spray pyrolysis technique, Thin Solid Films **480–481**, 439 (2005).

[54] M. Nagasawa and S. Shionoya, Exciton structure in optical absorption of SnO_2 crystals, Phys. Lett. **22**, 409 (1966).

[55] Y. Ogo, H. Hiramatsu, K. Nomura, H. Yanagi, T. Kamiya, M. Hirano, and H. Hosono, *p*-channel thin-film transistor

using *p*-type oxide semiconductor, SnO, Appl. Phys. Lett. **93**, 032113 (2008).

[56] V. Stevanović, K. Hartman, R. Jaramillo, S. Ramanathan, T. Buonassisi, and P. Graf, Variations of ionization potential and electron affinity as a function of surface orientation: The case of orthorhombic SnS, Appl. Phys. Lett. **104**, 211603 (2014).

[57] Y. Hinuma, A. Grüneis, G. Kresse, and F. Oba, Band alignment of semiconductors from density-functional theory and many-body perturbation theory, Phys. Rev. B **90**, 155405 (2014).

[58] V. Stevanović, S. Lany, D. S. Ginley, W. Tumas, and A. Zunger, Assessing capability of semiconductors to split water using ionization potentials and electron affinities only, Phys. Chem. Chem. Phys. **16**, 3706 (2014).

[59] A. Grüneis, G. Kresse, Y. Hinuma, and F. Oba, Ionization Potentials of Solids: The Importance of Vertex Corrections, Phys. Rev. Lett. **112**, 096401 (2014).

[60] W. Chen and A. Pasquarello, Band-edge positions in *GW*: Effects of starting point and self-consistency, Phys. Rev. B **90**, 165133 (2014).

[61] P. W. Tasker, The stability of ionic crystal surfaces, J. Phys. C **12**, 4977 (1979).

[62] *Thermodynamic Properties of Inorganic Materials Compiled by SGTE* (Springer, New York, 1990).

[63] V. Stevanović, S. Lany, X. Zhang, and A. Zunger, Correcting density functional theory for accurate predictions of compound enthalpies of formation: Fitted elemental-phase reference energies, Phys. Rev. B **85**, 115104 (2012).

[64] S. Shang, Y. Wang, P. Guan, W. Y. Wang, H. Fang, T. Anderson, and Z.-K. Liu, Insight into structural, elastic, phonon, and thermodynamic properties of α-sulfur and energy-related sulfides: A comprehensive first-principles study, J. Mater. Chem. A **3**, 8002 (2015).

[65] B. D. Malone, A. Gali, and E. Kaxiras, First principles study of point defects in SnS, Phys. Chem. Chem. Phys. **16**, 26176 (2014).

[66] S. T. Murphy and N. D. M. Hine, Anisotropic charge screening and supercell size convergence of defect formation energies, Phys. Rev. B **87**, 094111 (2013).

[67] R. E. Banai, L. A. Burton, S. G. Choi, F. Hofherr, T. Sorgenfrei, A. Walsh, B. To, A. Cröll, and J. R. S. Brownson, Ellipsometric characterization and density-functional theory analysis of anisotropic optical properties of single-crystal α-SnS, J. Appl. Phys. **116**, 013511 (2014).

[68] H. Yanagi, Y. Iguchi, T. Sugiyama, T. Kamiya, and H. Hosono, *N*-type conduction in SnS by anion substitution with Cl, Appl. Phys. Express **9**, 051201 (2016).

[69] S. Lany and A. Zunger, Anion vacancies as a source of persistent photoconductivity in II–VI and chalcopyrite semiconductors, Phys. Rev. B **72**, 035215 (2005).

[70] R. D. Shannon, Revised effective ionic radii and systematic studies of interatomic distances in halides and chalcogenides, Acta Crystallogr. Sect. A **32**, 751 (1976).